Quantum dot solar concentrators

© A.J. Chatten¶, K.W.J. Barnham, B.F. Buxton*, N.J. Ekins-Daukes+, M.A. Malik≠

Physics Department, Imperial College, London, SW7 2BW, U.K
* Computer Science Department, U.C.L., London, WC1E 6BT, U.K
+ Toyota Technological Institute, Nagoya, 468-8511, Japan
≠ Chemistry Department, University of Manchester, Manchester, M13 9PL, U.K

(Получена 9 февраля 2004 г. Принята к печати 11 февраля 2004 г.)

The luminescent properties of core-shell quantum dots are being exploited in an unconventional solar concentrator which promises to reduce the cost of photovoltaic electricity. Luminescent solar collectors have advantages over geometric concentrators in that tracking is unnecessary and both direct and diffuse radiation can be collected. However, development has been limited by the performance of luminescent dyes. We present experimental and theoretical results with a novel concentrator in which the dyes are replaced by quantum dots. We have developed a self-consistent thermodynamic model for planar concentrators and find that this three-dimensional flux model shows excellent agreement with experiment.

1. Introduction

The luminescent planar solar concentrator [1] was originally proposed in the late 1970 s. It consisted of a transparent sheet doped with appropriate organic dyes. Sunlight is absorbed by the dye and then re-radiated isotropically, ideally with high quantum efficiency and trapped in the sheet by internal reflection. A stack of sheets doped with different dyes [1] can separate the light, as in Fig. 1, and solar cells can be chosen to match the different luminescent wavelengths to convert the trapped light at the edge of the sheet.

Advantages over geometric concentrators include that expensive solar tracking is unnecessary and that both direct and diffuse radiation can be collected. However, the development of this promising concentrator was limited by the stringent requirements on the luminescent dyes, namely high QE, suitable absorption spectra and red-shifts and stability under illumination [2].

2. The quantum dot concentrator (QDC)

We have recently proposed a novel concentrator [3] in which the dyes are replaced by quantum dots (QDs). The first advantage of the QDs over dyes is the ability to tune the absorption threshold simply by choice of dot diameter. Secondly, high luminescence quantum efficiency has been observed. CdSe/CdS heterostructure dots have demonstrated luminescence quantum yields above 80% at room temperature [4]. Thirdly, since they are composed of crystalline semiconductor, the dots should be inherently more stable than dyes.

The disappointing results obtained with dye concentrators were probably mainly because of re-absorption, which was considered, but not modelled at the time of the original calculations [1]. Therefore, in [3] we have argued that there is a further advantage in that the red-shift between absorption and luminescence is *quantitatively* related by the thermodynamic model to the *spread* of quantum dot sizes, which can be determined during the growth process [5]. The ability to limit the overlap between the luminescence and absorption by the choice of QD size distribution is a significant improvement compared to dye concentrators allowing re-absorption losses to be minimised [6,7].

3. Thermodynamic modelling of the QDC

Yablonovitch [8] applied a detailed balance argument to the original dye-concentrator to relate the absorbed light and self-absorbed concentrated light to the spontaneous emission. The paper considers a uniformly illuminated thin slab, for which the variation of the incident light with depth is negligible. In a practical device however, a significant fraction of the incident flux is absorbed. Yablonovitch applies the boundary condition to the trapped flux that it is zero at the edge of the sheet and derives an expression for the flux propagating towards the cell. It is not possible using Yablonovitch's boundary condition to derive an expression for the flux propagating backwards that is consistent with that propagating forwards. The form of the detailed balance expression in [8] is again limited to thin sheets for which a negligible fraction of the radiation emitted into the escape cone may be re-absorbed by the sheet. This model does not consider losses owing to absorption by the „transparent" sheet material and we find that this is one of the most important factors limiting the efficiency of planar luminescent solar consentrators. Yablonovitch's one-dimensional model is also limited to the case where there is no spectral overlap of the incident radiation and the luminescence. To overcome these difficulties we have developed a self-consistent three-dimensional (3D) flux model in which we apply reflection boundary conditions to the radiation depending on whether if falls within the escape cone, Ω_c, or within the solid angle of total internal reflection in each co-ordinate direction x, y, z.

¶ E-mail: a.chatten@imperial.ac.uk
Fax: +44 (0) 20 7581 3817

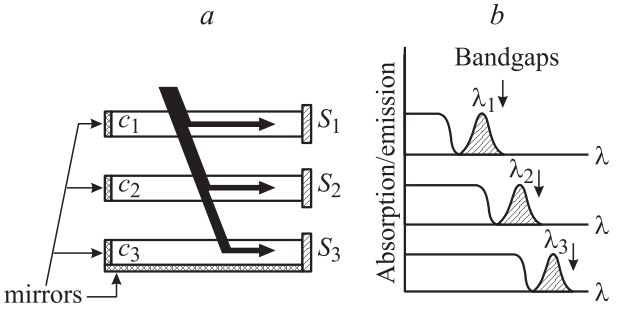

Figure 1. *a* — schematic of a three-stack luminescent concentrator. Each layer in the stack absorbs and re-emits light of longer wavelength with ideal absorption coefficient and luminescence spectra as in *b*.

Our 3D flux model allows for: 1) a significant fraction of the incident flux to be absorbed by the sheet, 2) spectral overlap of the incident radiation with the luminescence, 3) re-absorption of radiation emitted into the escape cone, 4) reflection at the surfaces, and 5) losses due to absorption in the host material. Including (1) to (5) can make an order of magnitude difference to the calculated luminescence escaping the right surface (see Fig. 1, *a*) compared to the predictions of [8], even for a small $42 \times 10 \times 5$ mm test slab. The model provides equations from which the photon chemical potential as a function of position within a finite slab of material may be determined by iteration.

4. 3D flux model

To obtain the differential equations describing the propagation of the trapped and escaping photon intensities, we start with Chandrasekhar's general three-dimensional radiative transfer equation [9]. We consider a finite slab of material of thickness D in the z direction, length L in the x direction and width W in the y direction, uniformly illuminated on (say) the top surface.

We apply the method of Schwarzschild and Milne [10], in which the detailed angular dependence of the radiative intensity described by the transfer equation is ignored and the radiation is considered as consisting simply of forward $(+)$ and backward $(-)$ streams. However, in addition, we also distinguish between what happens when the angle of propagation, θ, is greater or less than the critical angle θ_c. Escaping photons with $\theta < \theta_c$ and trapped photons with $\theta > \theta_c$ are treated as separate streams. We then integrate over the appropriate angular ranges to obtain the intensities of the photon streams and ignore other details of the angular dependence. Integrating over the escape cones in each co-ordinate direction produces two differential equations [6] for the luminescent escaping fluxes propagating in the positive and negative directions:

$$\mp \frac{\partial I_{x,y,z}^{(\pm)}}{\partial x, y, z} = \lambda_a I_{x,y,z}^{(\pm)} - \frac{\Omega_c}{4\pi} \lambda_e B. \qquad (1)$$

In equation (1) $I_x^{(\pm)}$, $I_y^{(\pm)}$ and $I_z^{(\pm)}$ are the escaping luminescent fluxes propagating within the slab in the positive and negative x, y and z directions respectively, and λ_a and λ_e are defined by:

$$\lambda_a = \frac{N\sigma_a(\nu)}{\cos^2(\theta_c/2)}, \qquad \lambda_e = \frac{N\sigma_e(\nu)}{\cos^2(\theta_c/2)}. \qquad (2)$$

Here, N is the density of luminescent centres, $\sigma_a(\nu)$ is the absorption cross section of the slab material comprising a transparent medium with absorption cross section $\sigma_b(\nu)$ within which the luminescent species with absorption cross section $\sigma_e(\nu) = \sigma_a(\nu) - \sigma_b(\nu)$ is uniformly dispersed. The luminescent brightness, B, of a radiation field in equilibrium with the electronic degrees of freedom of the absorbing species is given by

$$B(\nu) = \frac{8\pi n^2 \nu^2}{c^2} \frac{1}{\exp\left[(h\nu - \mu)\beta\right] - 1} \qquad (3)$$

where n is the refractive index, ν is the frequency, μ is the photon chemical potential, $\beta = 1/kT$, and the other quantities have their usual meaning. The incident radiation, I_1, is not distributed over the same angular range as the escaping luminescence and thus must be treated separately. If I_1 is incident at θ_i it generates escaping fluxes, $I_d^{(\pm)}$, within the slab which depend on z and the transmission angle, θ_t:

$$\mp \frac{\partial I_d^{(\pm)}}{\partial z} = \frac{N\sigma_a}{\cos\theta_t} I_d^{(\pm)}. \qquad (4)$$

4.1. Trapped intensity

Suitable transparent media generally have refractive indices close to 1.5. Thus the totally trapped solid angle $\Omega_6 = 4\pi - 6\Omega_c$ is small. The trapped intensity also equilibrates within the slab by multiple reflections and hence we may integrate the radiative transfer equation over this solid angle to obtain an average trapped intensity:

$$I_t^{(\cdot)} = \frac{N\sigma_e}{N\sigma_a} \frac{\Omega_6 B}{4\pi}. \qquad (5)$$

4.2. Detailed balance

Application of the principle of detailed balance within the slab of material leads to equation:

$$F(\mu) = \int d\nu \sigma_e(\nu) I_C(\nu) - \int d\nu \frac{\sigma_e(\nu)}{Q_e} B(\nu) = 0 \qquad (6)$$

where Q_e is the quantum efficiency of the luminescent species and $F(\mu)$ is minimised to determine μ. I_C is the concentrated photon field within the slab which is obtained by adding the total trapped and escaping intensities in the x, y and z directions:

$$I_C = I_t^{(\cdot)} + I_x + I_y + I_z + I_d. \qquad (7)$$

The escaping intensities are themselves given by adding the appropriate photon streams as in:

$$I_{x,y,z,d} = I^{(+)}_{x,y,z,d} + I^{(-)}_{x,y,z,d}. \tag{8}$$

Equation (6) shows that the variation of I_C with position in the slab is dependent on the variation of μ with position.

For thin films, the differential equations (1) may be solved analytically [7]. For thick slabs, we can only solve the differential equations up to integration over the slab of the luminescent brightness B multiplied by the appropriate forward and backward Green's functions [6].

4.3. Boundary conditions

For the luminescent escaping fluxes, $I^{(\pm)}_{x,y,z}$, we have to consider reflection and transmission at the surfaces. For example, at the left surface $x = 0$, the far surface $y = 0$ and the top surface $z = 0$ these are:

$$I^{(+)}_{x,y,z}(0) = B_{\mathrm{L,F,T}}\, I^{(-)}_{x,y,z}(0) \tag{9}$$

where $R_{\mathrm{L,F,T}}$ are the reflection coefficients averaged over the escape cone for the luminescent escaping fluxes at the left, far and top surfaces respectively. Similar boundary conditions on $I^{(\pm)}_{x,y,z}$ apply at the right surface $x = L$, the near surface $y = W$ and bottom surface $z = D$, with appropriate reflection coefficients $R_{\mathrm{R,N,B}}$ at the right, near and botton surfaces respectively. At the top and bottom we also have boundary conditions on the fluxes $I^{(\pm)}_d$:

$$I^{(+)}_d(0) = (1 - R_{\mathrm{Td}})I_1 + R_{\mathrm{Td}} I^{(-)}_d(0), \tag{10}$$

$$I^{(-)}_d(D) = R_{\mathrm{Bd}} I^{(+)}_d(D) \tag{11}$$

with reflection coefficients R_{Td} and R_{Bd} as required for the angle of incidence of the direct incident light.

In the x and y directions at the left (L), and far (F), surfaces, the boundary conditions for the luminescent escaping fluxes outside the slab are:

$$I_{\mathrm{L,F}} = (1 - R_{\mathrm{L,F}}) I^{(-)}_{x,y}(0) \tag{12}$$

with similar equations at the right (R), near (N), top (T), and bottom (B) surfaces. By integrating the differential equations for the escaping fluxes, evaluating the resulting expressions at the surfaces and applying the boundary conditions, we derive the escaping intensities. In carrying out these calculations, it is convenient, since the reflection coefficients lie in the range [0, 1], to rewrite the reflectivities as:

$$R_{\mathrm{P}} = e^{-\alpha_{\mathrm{P}}}, \qquad \alpha_{\mathrm{PQ}} = \frac{\alpha_{\mathrm{P}} + \alpha_{\mathrm{Q}}}{2} \tag{13}$$

where P, Q = L, R, F, N, T, B, Td, Bd.

4.4. Escaping intensities

The expressions for the luminescent escaping intensities within the slab in the x, y and z directions are related by symmetry. For example I_x is given by

$$I_x(x,y,z) = \frac{\Omega_c \lambda_e \cosh(\lambda_a x + \alpha_{\mathrm{L}}/2)}{2\pi \sinh(\lambda_a L + \alpha_{\mathrm{LR}})} \times \int_0^L dx' \cosh\left[\lambda_a (L - x') + \alpha_{\mathrm{R}}/2\right] B(x', y, z) - \frac{\Omega_c \lambda_e}{2\pi} \int_0^x dx' \sinh\left[\lambda_a (x - x')\right] B(x', y, z) \tag{14}$$

and the expressions for I_y and I_z are generated by replacing the co-ordinate, the slab dimension and the α subscripts in equation (14) with those appropriate for the direction of interest. The intensity, I_d, within the slab owing to unabsorbed incident radiation is diven by

$$I_d(z) = \frac{2I_1 \sinh(\alpha_{\mathrm{Td}}/2) \cosh\left[N\sigma_a (D - z)/\cos\theta_t + \alpha_{\mathrm{Bd}}/2\right]}{\sinh(N\sigma_a D/\cos\theta_t + \alpha_{\mathrm{TdBd}})}. \tag{15}$$

The expressions for the luminescent fluxes outside the slab escaping the surfaces in the x, y and z directions are again related by symmetry. For example the fluxes I_{R} and I_{L} escaping the right and left surfaces in the x direction respectively are:

$$I_{\mathrm{R}}(y,z) = \frac{\Omega_c \lambda_e}{2\pi} \frac{\exp(-\alpha_{\mathrm{LR}}) \exp(-\lambda_a L) \sinh(\alpha_{\mathrm{R}}/2)}{\sinh(\lambda_a L + \alpha_{\mathrm{LR}})} \times \int_0^L dx' \cosh\left[\lambda_a (L - x') + \alpha_{\mathrm{R}}/2\right] B(x', y, z) + \frac{\Omega_c \lambda_e \exp(-\alpha_{\mathrm{R}}/2) \sinh(\alpha_{\mathrm{R}}/2)}{2\pi} \times \int_0^L dx' \exp\left[-\lambda_a (L - x')\right] B(x', y, z), \tag{16}$$

$$I_{\mathrm{L}}(y,z) = \frac{\Omega_c \lambda_e}{2\pi} \frac{\sinh(\alpha_{\mathrm{L}}/2)}{\sinh(\lambda_a L + \alpha_{\mathrm{LR}})} \times \int_0^L dx' \cosh\left[\lambda_a (L - x') + \alpha_{\mathrm{R}}/2\right] B(x', y, z). \tag{17}$$

The expressions for I_{N} and I_{F} and the luminescent components of I_{B} and I_{T} are generated by appropriate substitution as for equation (14). The latter, I_{B} and I_{T}, are similar but

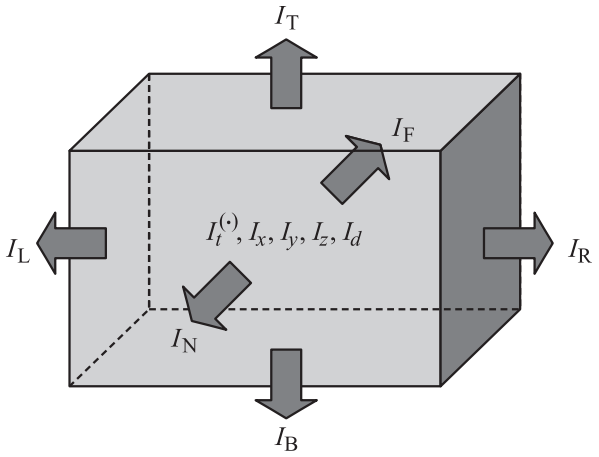

Figure 2. Schematic diagram illustrating the intensities within the slab comprising the concentrated intensity, I_C, and the fluxes escaping the surfaces.

contain additional terms arising from the incident flux:

$$I_B(\text{incident}) = I_1 \frac{2\sinh(\alpha_{Bd}/2)\sinh(\alpha_{Td}/2)}{\sinh(N\sigma_a D/\cos\theta_t + \alpha_{TdBd})}, \qquad (18)$$

$$I_T(\text{incident}) = I_1 \times \frac{\left[\exp(-\alpha_{Td}/2)\sinh(N\sigma_a D/\cos\theta_t + \alpha_{Bd}/2) + \exp(-\alpha_{Bd}/2)\exp(-N\sigma_a D/\cos\theta_t)\sinh(\alpha_{Td}/2)\right]}{\sinh(N\sigma_a D/\cos\theta_t + \alpha_{TdBd})}. \qquad (19)$$

The intensities comprising I_C within the slab (see Fig. 2) are calculated as outlined above by determining the chemical potential, $\mu(x, y, z)$, over a mesh of positions within the slab by Newton–Raphson iteration. This chemical potential distribution best satisfies the detailed balance condition (equation (6)) at each point in the slab and is then used to calculate the position dependent fluxes exiting the surfaces. In this calculation the Newton–Raphson equation below is solved iteratively for μ at each point in the mesh:

$$\mu_s = \mu_{s-1} - \frac{F(\mu_{s-1})}{F'(\mu_{s-1})} \qquad (20)$$

where we ignore the dependence of I_C on μ so that:

$$F'(\mu) \approx \int d\nu \, \frac{\sigma_e(\nu)}{Q_e} \frac{8\pi n^2 \nu^2}{c^2} \frac{\beta \exp[(h\nu - \mu)\beta]}{\{\exp[(h\nu - \mu)\beta] - 1\}^2}. \qquad (21)$$

5. Results

This section is divided into three parts. The first details experimental absorption and luminescence measurements, and the latter are shown to compare favourably with predictions from the model. The second section concerns modelling results and discusses the importance of the QD size distribution, the predicted fluxes exiting the surfaces of a slab and the photon chemical potential. In the third part predicted short-circuit currents resulting from the fluxes exiting the surfaces of sample slabs uniformly illuminated on their top surfaces are compared with experiment. These measurements show that the 3D flux model agrees with experiment, providing a tool for optimisation of the QDC.

5.1. Absorption and luminescence

Both the sample absorption and luminescence are measured on a wavelength calibrated double monochromator system, composed of two 30 cm Bentham monochromators. The source monochromator has a current stabilised 100 W tungsten filament lamp attached to a variable entrance slit. It is also equipped with order sorting filters, a 1800 lines/mm grating and an exit pinhole aperture of 200 μm. The wavelength resolution varies with entrance slit width but excitation wavelengths < 1 nm can be achieved. The spectrometer monochromator also has a pair of variable slits, a 1200 lines/mm grating and wavelength resolution of 2 nm. A calibrated Newport 818-UV silicon detector was used for all absorption and luminescence measurements as shown in Fig. 3 and 4.

Absorption measurements were performed in a parallel-beam configuration (see Fig. 3) by acquiring a transmission measurement on the sample and a reference measurement. The absorption coefficient, $N\sigma_a$, corrected for multiple reflections using equation (18) is extracted from the data. Scans were generally carried out over the wavelength range 400 to 800 nm under computer control with the output of the silicon detector amplified by a Stanford research systems SR510 lock-in amplifier and the monochromator driven by a Bentham PM C3B/IEEE controller. For absorption measurements light from the lamp was chopped before it entered the monochromator with

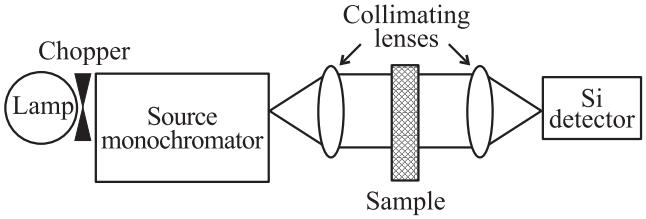

Figure 3. Apparatus used to measure the absorption properties of test slabs.

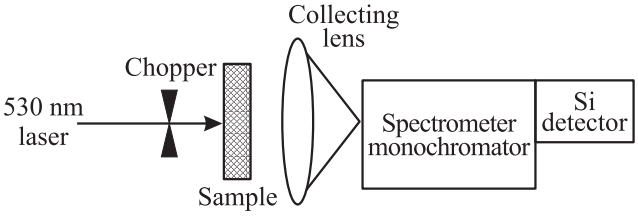

Figure 4. Apparatus used to measure the luminescence properties of test slabs.

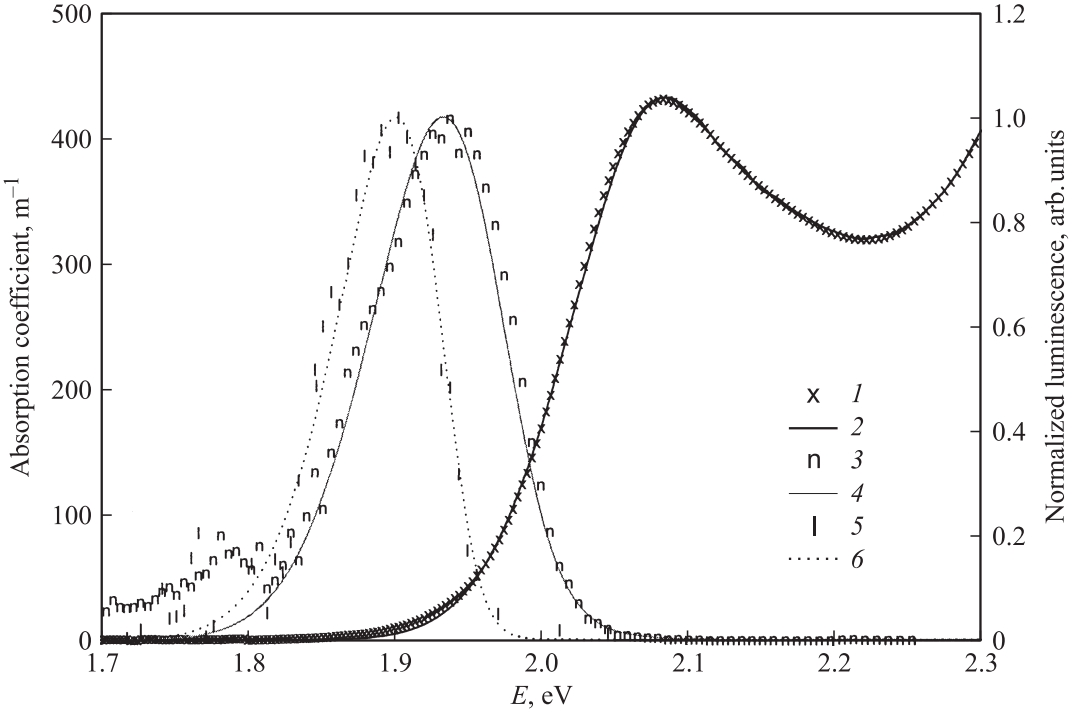

Figure 5. Measured absorption coefficient (*1*) and Gaussian fit (*2*) to the absorption threshold together with the normalised predicted and observed luminescence for the $L \times W \times D = 42 \times 10 \times 5\,\mathrm{mm}^3$ test slab of CdSe/CdS QDs in acrylic. For laser illumination on the near surface (*3*) indicates the predicted and (*4*) the observed luminescence. For laser illumination on the left surface (*5*) indicates the predicted and (*6*) the observed luminescence.

a Bentham 218 variable frequency chopper at a frequency of approximately 188 Hz which was suitably far away from the mains frequency of 50 Hz to produce good results.

Luminescence measurements were often performed with the straight-through configuration (see Fig. 4) and the light escaping the surface of the sample opposite the laser illumination was focused onto the entrance slit of the spectrometer monochromator and detected at the exit slit by the silicon detector. The luminescence scans were carried out over the relevant wavelength range, again under computer control, using a second chopper and monochromator controller. The luminescence signal was corrected for the throughput of the spectrometer by performing two additional scans firstly with the beam from the source monochromator focused into the spectrometer and secondly a reference scan as for the absorption measurements.

We assume that the frequency dependence of $\sigma_e(\nu)$ at threshold is Gaussian as expected for dots with δ-function density of states and Gaussian distributed diameters [3]. A Gaussian fits the experimental absorption very well down to threshold [6,7], as illustrated in Fig. 5 together with the predicted and observed luminescence escaping a test slab of CdSe/CdS core-shell QDs in acrylic illuminated by a 530 nm laser in the x and y co-ordinate directions. The laser spot (diameter 3 mm) was positioned in the centre of the face of the slab of material and the luminescence was collected from the opposite surface. The slab was rotated such that the laser illuminated the left surface at $x = 0$ and the near surface at $y = 0$.

Fig. 5 shows the excellent agreement between the shape and position (red-shift) of the predicted and observed luminescence for the two directions of laser illumination although a small laser feature interferes with the experiment between 1.7 and 1.8 eV.

With laser illumination of a slab the intensity and red-shift of the flux escaping the right surface, I_R, is very dependent on the position of laser excitation on the top surface. In an additional experiment the luminescence escaping the right surface of the sample slab of CdSe/CdS QDs in acrylic was measured as the laser spot was moved along the centre of the top surface. The same equipment as shown in Fig. 4 was used but the laser was positioned such that the beam was perpendicular to the collection optics. Fig. 6 shows both the variation of the predicted and observed luminescence escaping the right surface of the slab with laser illumination position x/L. Unfortunately, the collected signal was too noisy to detect at laser positions less than $x/L = 0.5$ since the path-length of the escaping luminescence is longer than in the straight-through configuration. It is easy to adapt the model to simulate laser excitation because the incident light term depends only on z and can simply be removed from the model at (x, y) positions where the laser is not illuminating the slab. These measurements show that the model predicts the correct trends for the red-shift, the

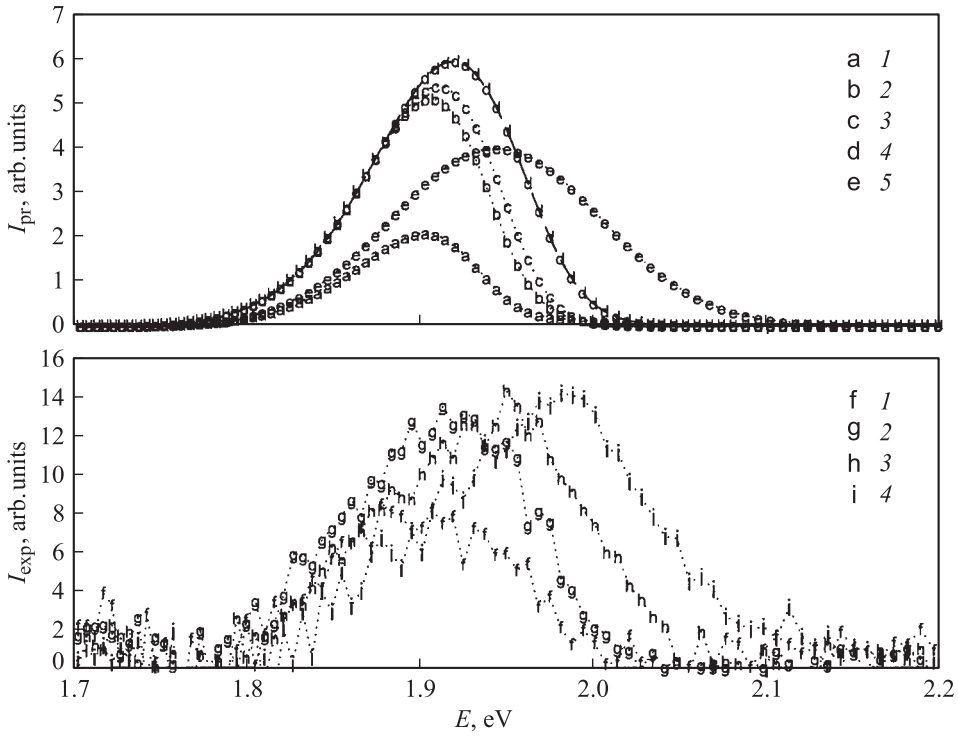

Figure 6. Variation of the predicted (I_{pr}) and observed (I_{exp}) luminescence escaping the right surface with the position of laser illumination on the top surface for the test slab of CdSe/CdS QDs in acrylic. In the calculations of the predicted luminescence (top chart) it was assumed that $Q_e = 0.5$ as determined from the photocurrent measurements. Simulations were carried out at laser positions x/L: *1* — 0, *2* — 0.25, *3* — 0.5, *4* — 0.75, *5* — 1. The bottom chart shows the experimental luminescence measured with the laser at positions x/L: *1* — 0.55, *2* — 0.76, *3*— 0.86, *4* — 0.95.

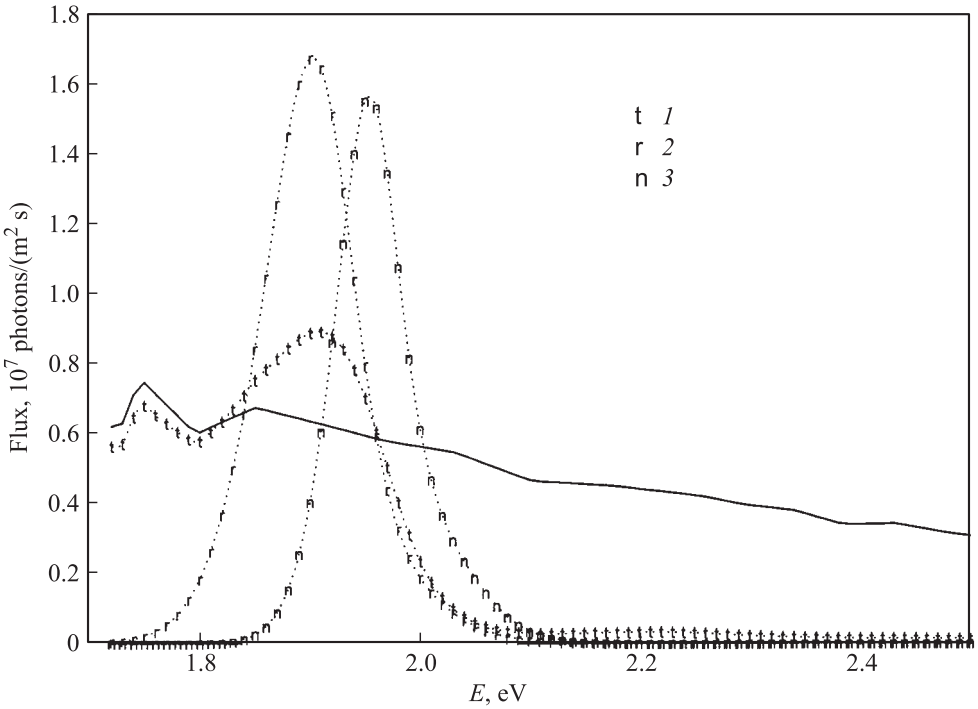

Figure 7. Predicted average fluxes escaping the top and right surfaces of the test slab of CdSe/CdS QDs in acrylic again assuming the best fit value of $Q_e = 0.5$. The slab has perfect mirrors at $x = 0$, $y = (0, W)$ and $z = D$, and is illuminated by AM1.5 at normal incidence. The solid line indicates the incident flux, *1* — the average flux escaping the top surface and *2* — the average flux escaping the right surface. The latter two escaping fluxes were both calculated using the Gaussian fit to the experimental absorption threshold with a half-width of 0.07 eV. Curve *3* illustrates the average flux escaping the right surface for a narrower QD size distribution modelled by a Gaussian fit of half-width 0.05 eV.

profile of the luminescence and its intensity as the laser position is varied. Compared to illumination at $x/L = 1$ we would expect the luminescence spectrum for illumination at $x/L = 0.95$ to be narrower owing to re-absorption and of higher intensity because more of the laser light can be absorbed.

5.2. Modelling results

The profile and red-shift of the luminescence peak also depends critically on the shape of the absorption cross section near threshold which reflects the QD size distribution. A narrower distribution of dot diameters can be modelled by narrowing the Gaussian fit to the absorption edge. The calculated fluxes escaping the surfaces for the test slab of CdSe/CdS core-shell QDs in acrylic assuming perfect mirrors at $x = L$ and $y = (0, W)$ are illustrated in Fig. 7 for the Gaussian fit (half-width 0.07 eV) to the experimental absorption. Fig. 7 shows the concentration of radiation into the flux that would be collected by a solar cell at the right surface. Also illustrated in Fig. 7 is the predicted flux escaping the right surface if the distribution of QD sizes were narrower such that the Gaussian fit to the absorption threshold has half-width 0.05 eV.

For a narrow distribution of QD sizes characterised by a sharp absorption threshold there is a smaller red-shift and therefore greater overlap with the luminescence, leading to larger re-absorption losses [6,7] and less radiation escaping the right surface. The model allows us to investigate quantitatively the distribution of dot diameters that minimises these losses. This is particularly important in our experiments since the luminescence quantum efficiency of the QDs in our test slab was rather low.

The chemical potential determined from the 3D flux analysis as a function of position, (x, y), for the CdSe/CdS QD sample slab with perfect mirrors at $y = (0, W)$ such that there is no variation of μ with y, is shown in Fig. 8. With no mirrors on the surfaces in the x direction the chemical potential is symmetric about $x = L/2$ and decreases with depth z allowing radiation of low energy photons near the bottom of the slab.

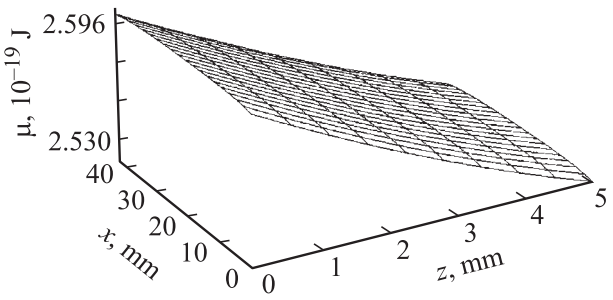

Figure 8. The position dependent chemical potential of the test slab of CdSe/CdS QDs in acrylic assuming $Q_e = 1$, perfect mirrors at $y = (0, W)$ and illumination by AM1.5 at normal incidence.

Table 1. Measured (top) and predicted (bottom) short circuit current, J_{sc}, using the 2.65×2.65 mm Si photodetector for the 3 unmirrored slabs investigated

Luminescent species	Slab size (mm)	Q_e	J_{sc} (mA/m^{-2})		
			$z = D$	$y = W$	$x = L$
CdSe/CdS QDs	$42 \times 10 \times 5$	0.50	84.0 ± 2.0 78.3 ± 1.9	4.6 ± 2.0 3.6 ± 0.8	11.1 ± 2.0 10.0 ± 1.4
Red dye	$40 \times 15 \times 3$	0.95	88.4 ± 2.0 85.4 ± 2.0	10.4 ± 2.0 11.1 ± 1.1	20.1 ± 2.0 22.0 ± 1.7
Green dye	$40 \times 15 \times 3$	0.95	93.2 ± 2.0 96.0 ± 2.1	3.2 ± 2.0 2.1 ± 0.3	4.9 ± 2.0 4.0 ± 0.9

Table 2. Measured (top) and predicted (bottom) short circuit current, J_{sc}, using the 3×3 mm GaAs photodetector for the red mirrored slab

Luminescent species	Slab size (mm)	Q_e	Blue filter used	J_{sc} (mA/m^{-2})
				$x = L$
Red dye	$40 \times 15 \times 3$	0.95	No	26.0 ± 2.0 26.0 ± 2.6
Red dye	$40 \times 15 \times 3$	0.95	Yes	12.7 ± 2.0 15.6 ± 2.1

Note. The reflectivity of the evaporated aluminium mirrors on the surfaces at $x = 0$, $z = D$ and $y = (0, W)$ was assumed to be 0.9. A blue filter could be placed between the lamp and sample to modify the spectrum of the light incident on the top surface of the slab.

5.3. Photocurrent measurements

Short circuit currents, J_{sc}, resulting from the radiation escaping the bottom, near and right surfaces of the slab of CdSe/CdS QDs in acrylic and slabs of red and green dyes in perspex were measured and are compared with the predicted values in Tables 1 and 2. The luminescence quantum efficiency, Q_e, of the perylene dyes is known to be about 0.95 and the unknown Q_e of the QDs was determined by the best fit to the experimental measurements.

The slabs were positioned on a matt black stage with a matt black background to avoid unwanted reflections and were illuminated at normal incidence by a calibrated Oriel fibre lamp. Two calibrated photodetectors that could be positioned against any surface were utilised to obtain J_{sc} values, using a Keithley 236 source measure unit. The uncertainty in the measurements is due to current generated by coupling of the incident light into the edges of the photodetector and allowance has been made for this by background measurements. The uncertainty in the predictions is mainly due to the 5% uncertainty in the experimental absorption.

The lamp spectrum was measured using the apparatus in Fig. 4 with the lamp focused into the entrance slit of the spectrometer monochromator. For the J_{sc} measurements the lamp was positioned such that light reaching the sample

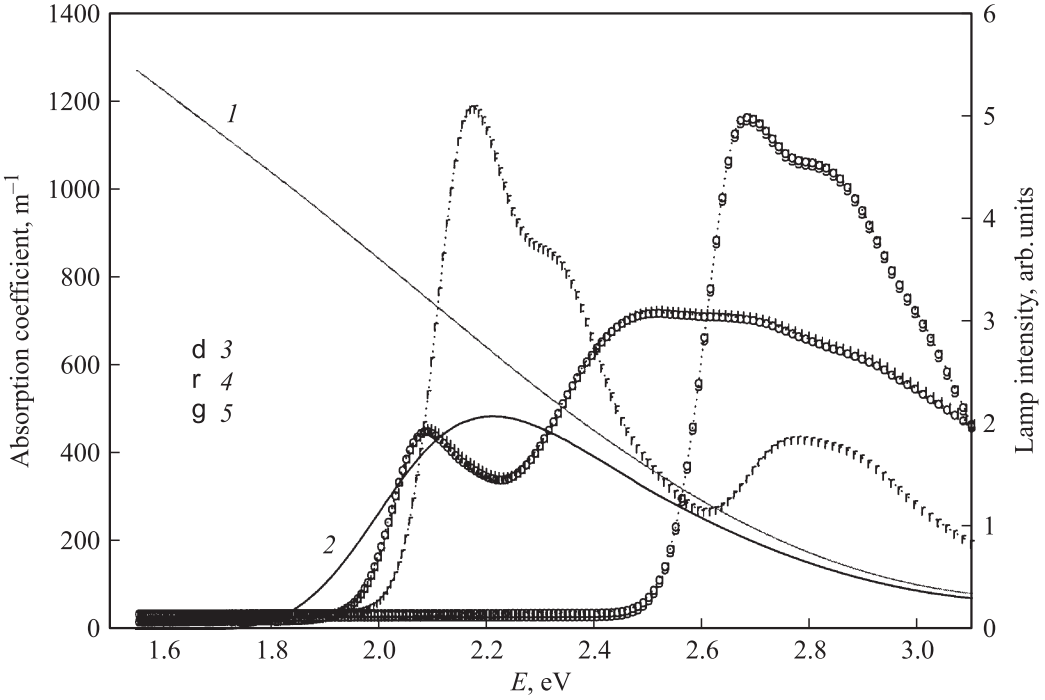

Figure 9. The Oriel lamp spectrum and effect of the blue filter together with the absorption spectra of the three materials investigated. Curve *1* is the Oriel spectrum and curve *2* shows how the incident light spectrum is modified when the blue filter is used. Curves with symbols *3*–*5* are the absorption: *3* — of the QDs in acrylic, *4* — of the red dye in perspex and *5* — of the green dye in perspex.

could only diverge by 5 degrees and corrections from normal incidence were negligible. The uniformity of the lamp illumination was checked and found to vary by less than 5% over the plane where the top surface of the test slab was positioned.

The quantum efficiency (QE) of the 2.65×2.65 mm Si photodetector and the 3×3 mm GaAs photodetector was determined with the apparatus in Fig. 3 by taking the ratio of a scan with the photodetector and a reference scan with the Newport 818-UV silicon detector corrected for its known QE. In order to calculate the predicted short-circuit currents it is necessary to correct for the angular dependence of the QE of the photodetector since the luminescence escapes at all angles over the hemisphere from each surface. The 2.65×2.65 mm Si photodetector was supplied with a correction curve and it would have been preferable to use this photodetector for all the measurements. However, it was not available at the time of the measurements on the mirrored red slab and these could not be repeated owing to poor adhesion of the evaporated aluminium mirrors. Therefore the same angular corrections were applied to the predictions of the short-circuit current from the 3×3 mm GaAs photodetector, leading to a greater uncertainty in these predictions.

The Oriel lamp spectrum and effect of the blue filter are illustrated together with the absorption coefficient, $N\sigma_a$, of the three materials in Fig. 9. It is very encouraging that all the measurements agree so well with the predictions given that the materials absorb strongly in different regions of the lamp spectrum and have very different losses owing to the high Q_e of the dyes and relatively low Q_e of the QDs. Our confidence in the model is also increased by the agreement with experiment for the slab with mirrored surfaces and the continued agreement when the spectrum of the light incident on the test slab is altered by a blue filter.

6. Conclusions

We have developed a self-consistent thermodynamic model for planar solar concentrators which allows for overlap of the incident radiation with the luminescence, for reflections at the surfaces, for re-absorption and for absorption losses in the „transparent“ host material. Our 3D flux model was derived by applying the method of Schwarzschild and Milne to Chandrasekhar's general radiative transfer equation coupled to a detailed balance condition. We can predict the efficiencies of luminescent concentrators using only the absorption properties of the slab, its refractive index, and the quantum efficiency Q_e of the luminescence. The QD size distribution can be chosen to *optimise* the red-shift and *minimise* the overlap between absorption and luminescence which is a significant advantage for the QDC compared with the dye concentrator. Our results show that the 3D flux model can predict both the red-shift and profile of the luminescence as well as the total flux escaping each surface of a slab providing a tool for optimisation of the QDC.

Acknowledgements

The authors would like to thank BP Solar, Saint-Gobain, the EPSRC and the European Commission (sixth framework program Integrated Project FULLSPECTRUM contract no. SES6-CT-2003-502620) for financial support. We are grateful to Dave Bushnell for his control software and have benefited from discussions of radiative transfer with Simon Arridge.

References

[1] A. Goetzberger and W. Greubel. Appl. Phys., **14**, 123 (1977).
[2] A. Goetzberger, W. Stahl, V. Wittwer. *Proc. 6th Eur. Photovolt. Solar Energy Conf.* (Reidel, Dordrecht, 1985) p. 209.
[3] K.W.J. Barnham, J.L. Marques, J. Hassard and P. O'Brien. Appl. Phys. Lett., **76**, 1197 (2000).
[4] A.P. Alivisatos. MRS Bulletin (February 18, 1998).
[5] O.I. Micic, C.J. Curtis, K.M. Jones, A.J. Nozik, J.R. Sprague. J. Phys. Chem., **98**, 4966 (1994).
[6] A.J. Chatten, K.W.J. Barnham, B.F. Buxton, N.J. Ekins-Daukes, M.A. Malik. *Proc 17th Eur. Photovolt. Solar Energy Conf.* (Munich, Germany, 2001) p. 200.
[7] A.J. Chatten, K.W.J. Barnham, B.F. Buxton, N.J. Ekins-Daukes, M.A. Malik. Sol. Energ. Mats. & Solar Cells, **75**, 363 (2003).
[8] E. Yablonovitch. J. Opt. Soc. Amer., **70**, 1362 (1980).
[9] S. Chandrasekhar. *Radiative Transfer* (Clarendon, Oxford, UK, 1950).
[10] E.A. Milne. Monthly Notices Roy. Astron. Soc. London, **81**, 361 (1921).

Редактор Т.А. Полянская